Quantifying the intensity of crystallographic preferred orientation (CPO): some practical considerations and recommended practices

A. J. Cross[1*]

[1]*Department of Geology and Geophysics, Woods Hole Oceanographic Institution, Woods Hole, MA, USA*

Corresponding author (e-mail: across@whoi.edu)

Abstract

Crystallographic preferred orientations (CPOs) commonly develop during the crystal-plastic deformation of rocks and minerals and are widely used to infer strain intensity and geometry, reconstruct deformation conditions, and estimate mechanical anisotropy. Numerous methods have been proposed to quantify CPO intensity as a scalar metric, but these metrics can be highly sensitive to their calculation parameters and input data quality. Here, we examine the performance of two widely used metrics—the J-index and the M-index—using orientation data from electron backscatter diffraction (EBSD) for a diverse suite of simulated, natural, and experimental specimens. We show that ODF-based measures of CPO intensity, such as the J-index, can vary markedly with kernel parameters and may fail to converge to a unique value. In contrast, the M-index, when calculated from random-pair misorientation angle histograms, yields stable, reproducible results across a broad range of conditions. Monte Carlo resampling demonstrates that M can be accurately described with 95% probability using ~500 orientations for moderate-to-strong CPOs ($M \geq 0.25$), whereas weak CPOs ($M < 0.1$) may require up to ~3,000 unique orientation measurements. These findings form the basis of a recommended, standardised practice to ensure that CPO intensity values are both reproducible and comparable across similar geological and experimental contexts.

1. Introduction

At elevated pressures and temperatures, rocks, minerals, and other crystalline materials often deform via crystal-plastic mechanisms that produce a rotation and/or alignment of their constituent crystals. For instance, when deformation is mediated by dislocation motion, grains will rotate into orientations that maximize dislocation glide and the shear stresses resolved on their weakest crystal lattice planes (Andrade & Roscoe, 1937), producing a crystallographic preferred orientation (CPO) defined by the alignment of certain crystal axes. While CPO development is often attributed to deformation by dislocation creep (e.g., Tullis, 1979; Karato, 1988; Fliervoet et al., 1999), there is also a growing body of literature demonstrating that modest CPOs may develop during dislocation-accommodated grain boundary sliding (disGBS) in olivine (Hansen et al., 2011; Precigout & Hirth, 2014), quartz (Cross et al., 2017a), calcite (Rutter et al., 1994; Pozzi et al., 2019; Demurtas et al., 2019), ice (Thomas et al., 2024), and plagioclase (Miranda et al., 2016). In contrast, deformation via diffusive mass transfer is often found to systematically weaken, or perhaps even entirely randomize, a pre-existing CPO (Boullier & Guergen, 1975; Zhang et al., 1994; Wheeler et al., 2009; Cross & Skemer, 2017), although several exceptions to this have also been identified (Bons & den Brok, 2000; Barreiro et al., 2007; Sundberg & Cooper, 2008; Miyazaki et al., 2013; Soda et al., 2019).

Regardless of the precise mechanisms responsible for their development, CPOs exert a major influence over the mechanical properties and geophysical signatures of deformed rocks. Given that CPOs typically arise from the alignment of easy-slip crystal lattice planes during deformation, the presence of a strong CPO can impart significant viscous anisotropy, where a material flows more readily in certain orientations than in others. Polycrystalline olivine, for instance, is up to ~15 times weaker when deformed in an orientation that maximizes shear stress on the (010)[100] slip system, versus in an orientation normal to that slip system (Hansen et al., 2012). Similarly, "enhancement" factors of up to 17 have been found for polycrystalline ice deforming via basal (0001) slip (Shoji & Langway Jr., 1988). Thus, CPO development is widely thought to impart progressive weakening—and influence strain localization—during the viscous flow of Earth's lithosphere (e.g., Bystricky et al., 2000; Skemer et al., 2013) and cryosphere (e.g., Azuma, 1994; Fan et al., 2021a). Meanwhile, CPOs also produce elastic anisotropy that gives rise to seismic anisotropy, a common means for inferring the magnitude and direction of viscous flow in ice sheets (e.g., Smith et al., 2017), the lower crust (e.g., Mainprice & Nicolas, 1989), and the upper mantle (see Karato et al., 2008; Skemer & Hansen, 2016).

2. CPO intensity metrics: The *J*- and *M*-index

Given the rheological, structural, and geophysical importance of mineral anisotropy, there has long been interest in quantifying CPO intensity, and its evolution, in exhumed natural shear zones and in experimental specimens. Although a population of crystal orientations can, most accurately, be described using a continuous, harmonic, probability density function—the orientation density function (ODF)—it is often desirable to represent CPO strength using a single, scalar value. Arguably the most widely used of these metrics is the *J*-index, defined as the L^2-norm of the ODF or, in plainer terms, as the sum of the squared orientation density (intensity) over the ODF (Bunge, 1982):

$$J_{\mathrm{ODF}} = \|f\|_{L^2}^2 = \int |f(g)|^2 \, \mathrm{d}g \tag{1}$$

where $f(g)$ represents the ODF for a population of orientations, g. The J-index ranges from 1 for a random (i.e., uniform) ODF to infinity for a single orientation, and can therefore be ambiguous in terms of what qualifies as a "strong" or "weak" CPO. Furthermore, as lower symmetry crystal systems occupy a larger volume of orientation space (as defined, for example, using three Euler angles), low-symmetry (e.g., triclinic) phases will necessarily exhibit larger values of J than high-symmetry (e.g., cubic) phases, unless a correction is made for the difference in ODF volume (e.g., Mainprice et al., 2015).

As an alternative, Skemer et al. (2005) proposed the misorientation index, M-index, defined as the difference between the random-pair (uncorrelated) misorientation-angle distribution (MAD) expected for a random orientation population of a given crystal symmetry class, R^0, and the random-pair MAD measured for a given sample, R^T:

$$M = \frac{1}{2}\int |R^T(\theta) - R^0(\theta)|\,\mathrm{d}\theta \qquad (2)$$

where θ is misorientation angle. As a reminder for the casual reader—if such a person exists for a paper as niche as this—the random-pair MAD is obtained by calculating the misorientation angle between every possible pair of orientations in a particular population, as opposed to the neighbour-pair MAD, which uses the misorientation angle only between orientation pairs measured adjacent to one another in Euclidean (sample coordinate) space. Thus, as CPO develops and grains become more strongly aligned, their random-pair MAD will progressively deviate from the theoretical MAD by migrating towards smaller misorientation angles (Wheeler et al., 2001). The *M*-index varies from 0 for a randomly oriented aggregate (i.e., with complete overlap between R^0 and R^T) to 1 for a single orientation (i.e., with no overlap between R^0 and R^T).

In its original form, the M-index was calculated using a histogram of the random-pair MAD—that is, with measurements discretized into bins of a finite width, typically 1° (Skemer et al., 2005):

$$M_{\mathrm{MAD}} = \frac{\theta_{\max}}{2n} \sum_{i=1}^{n} \left| R_i^T - R_i^0 \right| \mathrm{d}\theta \tag{3}$$

where $\theta_{\max}$ is the maximum misorientation angle for a given crystal symmetry class, and *n* is the number of bins. While Skemer *et al.* demonstrated that the *M*-index is insensitive to bin width up to (and including) a bin size of 40°, Mainprice et al. (2015) proposed an alternative, continuous form of the *M*-index, M_{ODF}, calculated from the measured and uniform ODFs, $f^{\mathrm{M}}(\theta)$ and $f^{\mathrm{U}}(\theta)$, respectively:

$$M_{\mathrm{ODF}} = \frac{1}{2} \int \left| f^{U}(\theta) - f^{M}(\theta) \right| \mathrm{d}\theta \tag{4}$$

It is this formulation of the *M*-index that is currently implemented in the widely used open-source MTEX toolbox (Bachmann et al., 2010).

3. Objectives

The main purpose of this contribution is to examine the sensitivity of common CPO intensity metrics—specifically, the *J*-index and *M*-index—to their calculation parameters and input data; first using synthetic data, and then using real data from a diverse selection of natural and experimental specimens containing major rock-forming minerals of various crystal symmetry classes. While other scalar representations of CPO intensity have been proposed—based on eigenvalue decomposition of the ODF (Woodcock, 1977; Vollmer, 1990) or on maximum pole figure intensity, for example—these methods provide an incomplete view of CPO intensity as they must be calculated for individual crystal axes rather than for the ODF as a whole.

This work is motivated by questions posed to the author by various electron backscatter diffraction (EBSD) users over the past decade or so regarding seemingly anomalous or disparate CPO intensity measurements. Nevertheless, the results presented herein should be applicable to orientation data obtained using any microanalytical or numerical method from which the complete crystal orientation is derived (e.g., excluding polarized-light analyses from which only the optic-axis orientation is provided). While CPO intensity comparisons among phases of different crystal systems are ill advised—as CPO "intensity" is highly sensitive to crystal symmetry—some recommended practices are suggested to encourage a more standardized reporting and comparison of CPO evolution across different studies and among like-phases.

4. Performance of the J- and M-indices for synthetic data

4.1. Single-crystals

As a starting point, we can examine how the *J*-index and *M*-index respond to the end-member case of a monodisperse (i.e., single-crystal) orientation distribution. Figure 1 shows J_{ODF} and M_{ODF} as a function of ODF halfwidth and bandwidth for several crystal-symmetry classes. The halfwidth—defined as the half-width at half-height of the kernel function used to construct the ODF—dictates the "sharpness" of the ODF. Larger halfwidth values emphasize broad, long-wavelength features, whereas smaller halfwidth values provide more sensitivity to local, short-wavelength features. Bandwidth, meanwhile, represents the highest harmonic order (i.e., highest angular-frequency band) used to construct the ODF. Contoured pole figures constructed using various ODF halfwidths and bandwidths are shown in Supplementary Figure S1 as an example, along with their spectral power distributions (i.e., harmonic decomposition showing the power of each Fourier coefficient).

As bandwidth increases, the number of terms used to fit the ODF to a population of orientations increases, allowing local variations in orientation density to be captured with greater fidelity. Generally speaking, more harmonic terms are required to describe an ODF constructed with a smaller halfwidth. In Figure 1, regions where the ODF is oversmoothed—defined here as conditions under which the three highest-order bands contain no information (*i.e.*, spectral power = 0)—are shaded in grey. In these regions, J_{ODF} and M_{ODF} fail to capture the intensity of the high-frequency components, and are therefore underestimated.

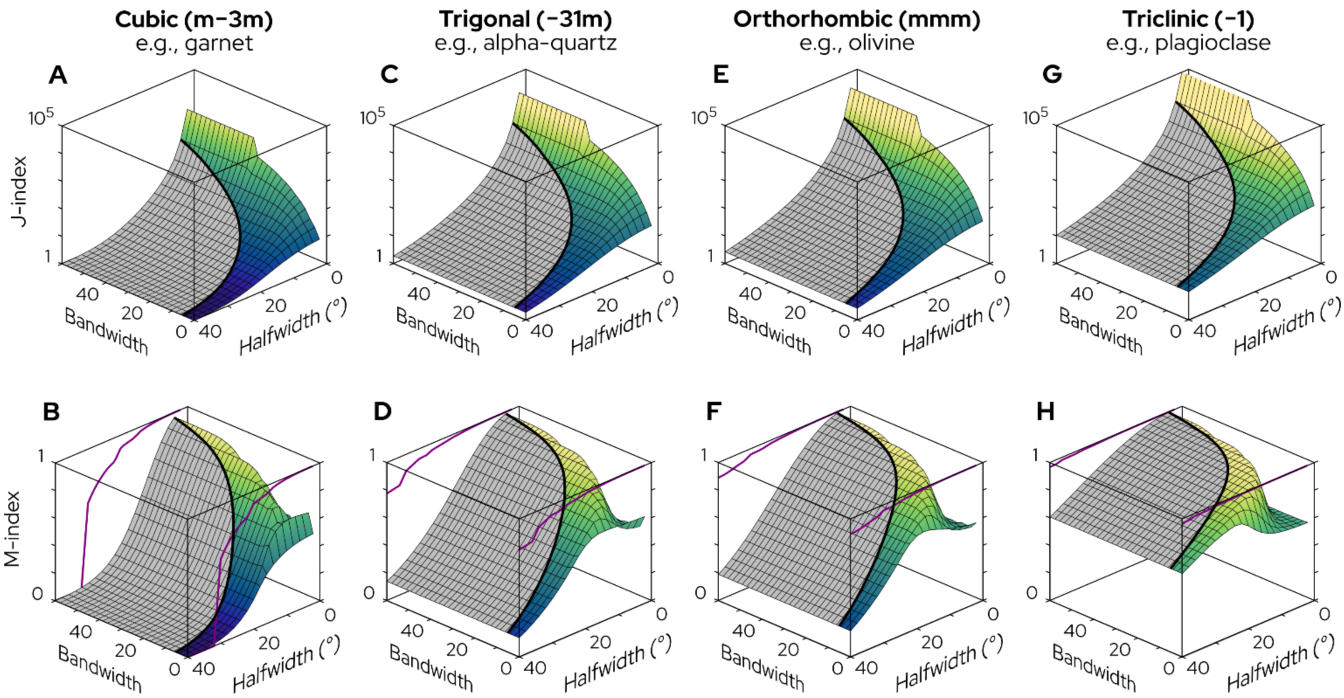

Figure 1: *J*-index (top row; Equation 1) and *M*-index (bottom row; Equation 4) as a function of ODF bandwidth and halfwidth for single orientations of A–B) cubic, C–D) trigonal, E–F) orthorhombic, and G–H) triclinic phases. Regions of parameter space where the ODF is oversmoothed (three highest-order bands contain no information) are shaded in grey. M_{ODF} and J_{ODF} are underestimated in these regions. All ODFs were constructed in MTEX using the default de la Vallee Poussin kernel (Schaeben, 1997). *M*-index values were also calculated using the original, discrete method of Skemer et al. (2005; Equation 3), and are plotted as 1-D curves (purple lines) alongside the M_{ODF} surfaces—for these values, the horizontal axis corresponds to the bin width of the misorientation angle histogram, rather than the ODF halfwidth.

As demonstrated by Skemer et al. (2005), J_{ODF} varies continuously over the entire parameter space, being relatively insensitive to bandwidth but highly sensitive to the ODF kernel halfwidth. At large halfwidth values (20–40°), J_{ODF} approaches unity; that is, the value expected for a random CPO (recall that these calculations are for monodisperse, single-crystal CPO). However, as halfwidth decreases to 2°, J_{ODF} increases over several orders of magnitude. The maximum magnitude of J_{ODF} also increases as crystal symmetry decreases, from 10^4 for cubic crystals to 10^5 for triclinic crystals, highlighting that CPO intensity cannot easily be compared among phases belonging to different crystal systems unless extra care is taken to normalize the results (Mainprice et al., 2015).

While the *M*-index was originally designed to avoid the shortcomings (i.e., non-uniqueness) of the *J*-index (Skemer et al., 2005), the *M*-index as currently implemented in MTEX—that is, being derived from the ODF (Equation 4) rather than from the MAD (Equation 3)—remains similarly sensitive to the ODF halfwidth and bandwidth (Figure 1). Notably, M_{ODF} is significantly underestimated for halfwidths exceeding 20°, and even for halfwidths in the range 5–15°, falling 7–56% below the true value of $M = 1$ for cubic crystals, and 2–25% below $M = 1$ for orthorhombic and trigonal crystals. As halfwidth values of 5–15° are commonly used to calculate ODFs and, thereby, produce contoured pole figures, it is likely that M_{ODF} is widely underestimated when calculated from those same ODFs. Values close to $M_{ODF} = 1$ are obtained only as the ODF halfwidth approaches 2°, yet drop off precipitously at smaller halfwidth values unless a very large bandwidth (>>50) is used. In contrast, we find that the original, discrete formulation of the *M*-index (Equation 3) is relatively stable, providing $M_{MAD} \approx 1$ so long as the MAD bin width does not exceed 10° (purple curves on Figure 1, bottom row). The discrete, MAD formulation is therefore more robust—and considerably more computationally efficient—at least for this simple test case.

4.2 Numerical polycrystals

To produce more broadly applicable results, we can now examine CPO intensity for a polycrystalline aggregate featuring varying degrees of crystallographic alignment. Figures 2 and 3 show how *J* and *M* evolve with increasing strain in numerical aggregates of olivine (Figure 2) and ice (Figure 3) subjected to simple-shear deformation using the viscoplastic self-consistent (VPSC) model of Lebensohn & Tomé (1993). The goal of these models is not to produce a fully realistic simulation of CPO evolution—that has been achieved elsewhere using more sophisticated analyses (e.g., Boneh et al., 2015; Hansen et al., 2016; Rathmann et al., 2024)—but, rather, to produce CPOs that span the range from random ($M = 0$; $J = 1$) to strongly unimodal ($M \rightarrow 1$; $J \rightarrow \infty$). Slip systems and critical resolved shear stresses (CRSS) were chosen to promote the formation of a strong A-type $(010)[100]$ CPO in olivine, and a strong basal-⟨a⟩ $(0001)\langle\bar{1}2\bar{1}0\rangle$ CPO in ice: both commonly observed in natural settings. Olivine CPO evolution was modelled using the following slip systems: $(010)[100]$, $(001)[100]$, $(010)[001]$, $(100)[001]$, $\{021\}[100]$, $\{110\}[001]$, $\{110\}[110]$, and $\{031\}[113]$, with normalized critical resolved shear stresses (CRSS) of 1, 1, 2, 3, 6, 6, 10, and 10, respectively. The first six slip systems were chosen to satisfy von Mises' criterion, following Boneh et al. (2015) and Tomassi et al. (2000); the latter two slip systems were added to strengthen the A-type CPO and enable model convergence at large strains. Ice CPO evolution was modelled using the following slip systems: $c(0001)a\langle\bar{1}2\bar{1}0\rangle$, $m\{\bar{1}010\}a\langle\bar{1}2\bar{1}0\rangle$, and $\{11\bar{2}2\}\langle11\bar{2}\bar{3}\rangle$, with CRSS values of 1, 20, and 200, respectively, following Castelnau et al. (1996). VPSC simulations were conducted for 20,000 grains—far exceeding the population size needed to obtain a robust estimate of CPO intensity, as shown below—with no neighbour-grain interactions (i.e., co-rotation), and using tangent linearization to validate the Eshelby-type VPSC inclusion scheme (Molinari et al., 1987).

Figures 2 and 3 show many of the same trends discussed above. At any given strain, J_{ODF} and M_{ODF} decrease with increasing ODF halfwidth (Figures 2D–E, 3D–3E) as the ODF increasingly fails to capture short-wavelength (i.e., low misorientation angle) features (Figures 2C, 3C). In contrast, M_{MAD} monotonically increases along the same trajectory for all MAD bin widths ≤ 10°, spanning the expected range of 0 → 1. In general, M_{ODF} provides values of $M_{ODF} \approx M_{MAD}$ for ODF halfwidths of 2–5°. However, these solutions are relatively unstable, with M_{ODF} decreasing significantly at ODF halfwidths outside of this range (Figures 2E, 3E) and M_{ODF} even oscillating with increasing shear strain for a kernel halfwidth of 1° due to resonance of the ODF at large misorientation angles—note the small peaks in the misorientation distribution function (MDF) at angles ≥ 20° (dark blue curve, Figure 3C).

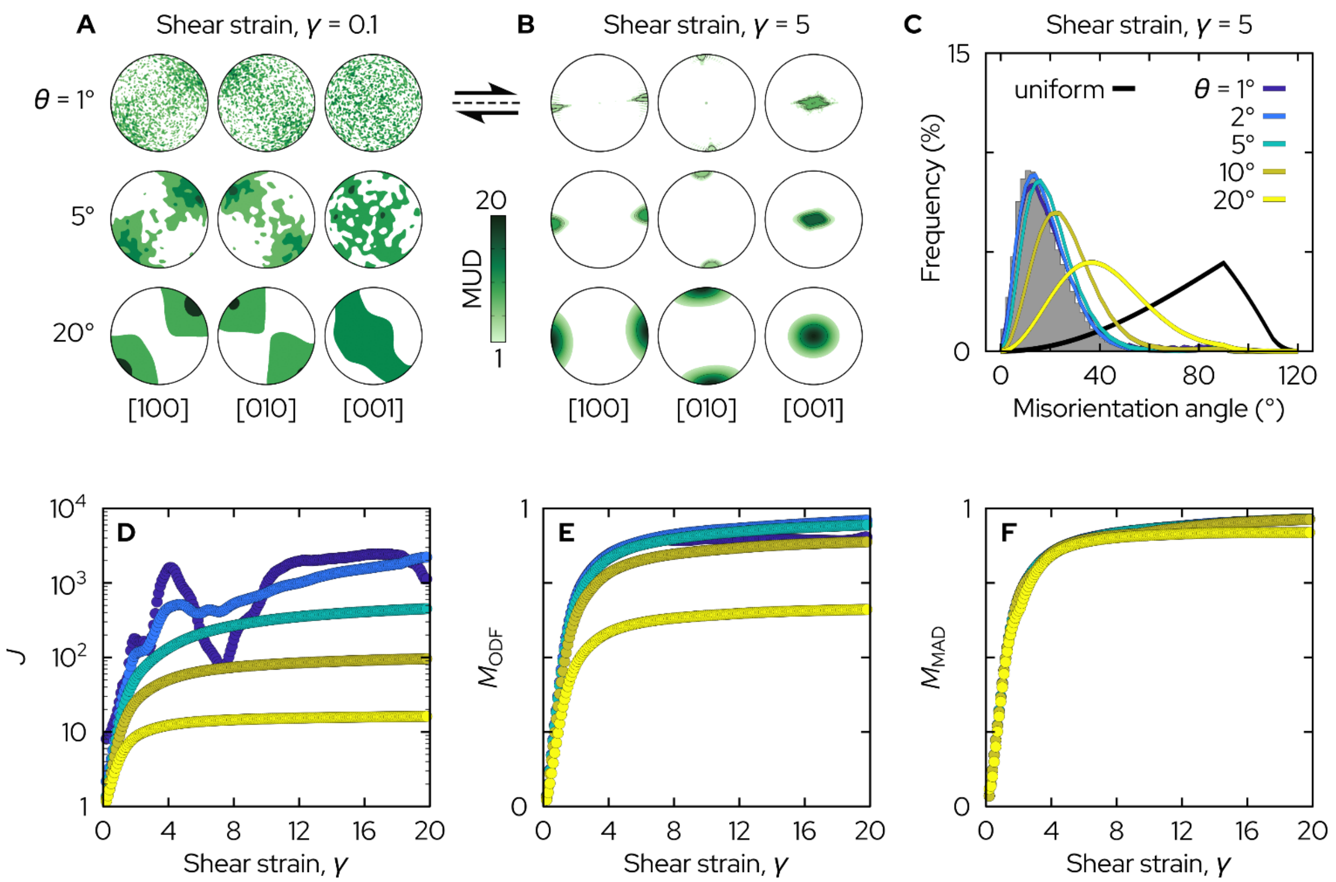

Figure 2: CPO evolution in numerical olivine aggregates undergoing simple shear deformation (see main text for details). (A-B) Contoured pole figures of the [100], [010], and [001] axes at shear strains of (A) γ = 0.1 and (B) γ = 5.0, produced using ODF kernel halfwidths of θ = 1°, 5°, and 20°. (C) The neighbour-pair misorientation angle distribution (MAD) at γ = 5.0 (grey histogram; 2° bin width), alongside misorientation angle functions (MDFs) constructed from ODFs with halfwidths of θ = 1–20°. Note that the MDFs provide a poor description of the MAD at $\theta \geq$ 10°. (C–E) The J-, M_{ODF}-, and M_{MAD}-indices as a function of strains for (C–D) ODF halfwidths of 1–20° and (E) MAD bin widths of 1–20°.

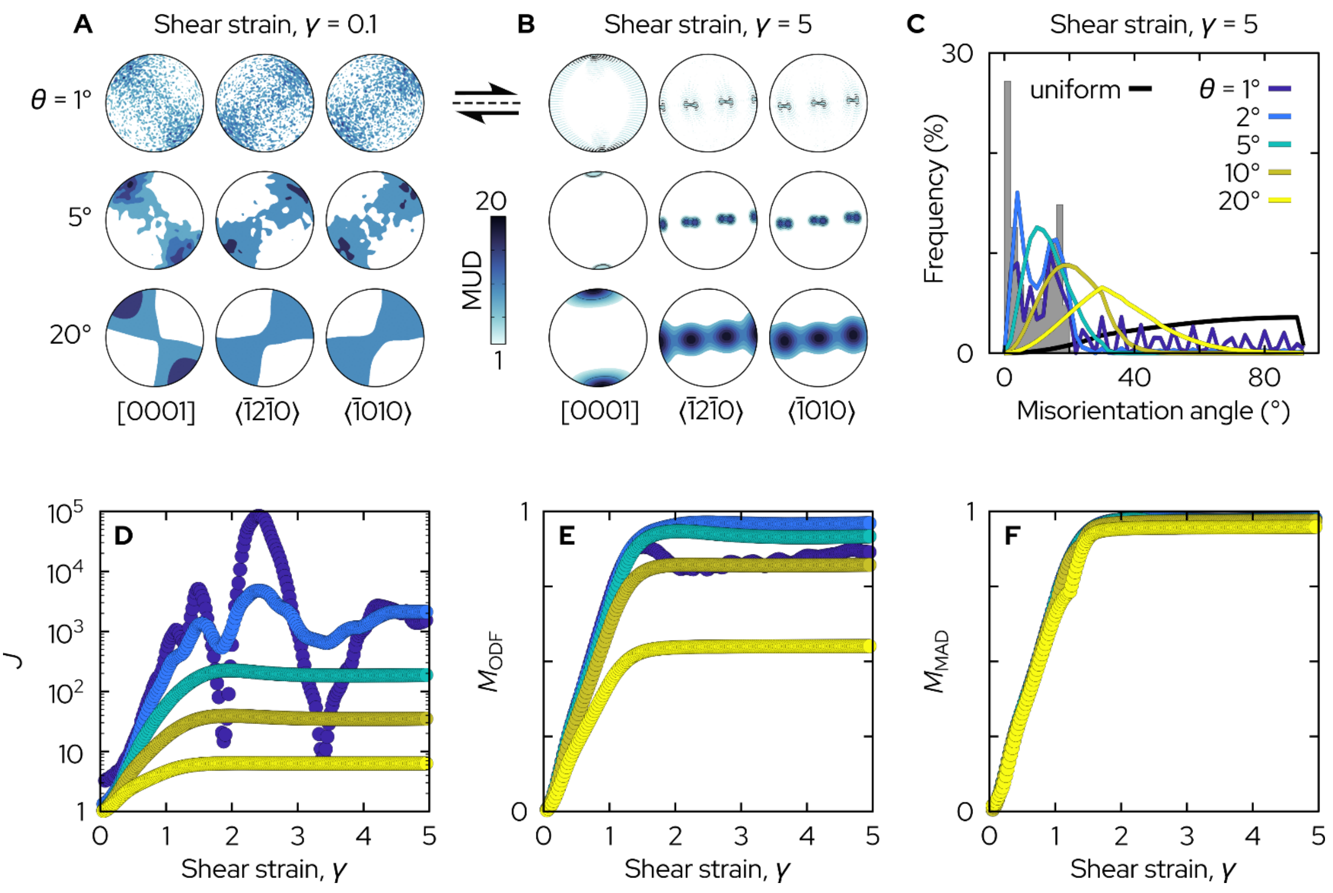

Figure 3: CPO evolution in numerical ice aggregates undergoing simple shear deformation (see main text for details). (A-B) Contoured pole figures of the [0001], ⟨$\bar{1}2\bar{1}0$⟩, and ⟨$\bar{1}010$⟩ axes at shear

strains of (A) $\gamma = 0.1$ and (B) $\gamma = 5.0$, produced using ODF kernel halfwidths of $\theta = 1°$, 5°, and 20°. (C) The neighbour-pair misorientation angle distribution (MAD) at $\gamma = 5.0$ (grey histogram; 2° bin width), alongside misorientation angle functions (MDFs) constructed from ODFs with halfwidths of $\theta = 1–20°$. Note that the MDFs provide a poor description of the MAD at $\theta \geq 5°$. (C–E) The *J*-, M_{ODF}-, and M_{MAD}-indices as a function of strains for (C–D) ODF halfwidths of 1–20° and (E) MAD bin widths of 1–20°.

5. One point per grain or all points?

When working with spatially resolved orientation data, another key consideration is whether to use all of the available data or just one representative measurement per grain (for example, the mean grain orientation). In general, it is common practice to construct pole figures using only the one-point-per-grain data, particularly in specimens with bimodal grain sizes (e.g., porphyroclastic mylonites) to avoid obscuring the overall CPO with the orientations of just a handful of large grains (e.g., Figure 4). Conversely, the all-points data are useful when the area- or volume-weighted data have important physical meaning—for example, when calculating the bulk elastic (seismic) anisotropy of a given specimen.

Similarly, CPO intensity can be calculated using the all-points or one-point-per-grain data. To illustrate the impact of this decision, we can examine a specimen with a strongly bimodal grain size. Sample DR538-R3, shown in Figure 4a, is an abyssal peridotite ultramylonite from the St. Paul's oceanic transform fault in the equatorial Atlantic Ocean. The sample was collected using a human-occupied vehicle during cruise AL170602 onboard the MV *Alucia*, and is composed primarily of olivine, pyroxene, amphibole, spinel, and low-temperature serpentinization and carbonation products (Klein et al., 2024). The sample was mapped using a Zeiss Supra 40VP SEM equipped with an Oxford Instruments Symmetry S1 detector at the Marine Biological Laboratory (Woods Hole, MA, USA). For the most part, DR538-R3 is fine-grained with a strong A-type CPO, attributed to dislocation glide on the (010)[100] slip system. However, the mapped portion of DR538-R3 also contains two large olivine porphyroclasts that cover 10% of the scanned region.

Figures 4B and 4C show random-pair (uncorrelated) misorientation angle histograms and contoured pole figures constructed using the all-points (Figure 4B) and one-point-per-grain (Figure 4C) data for sample DR538-R3. Note that in both cases, a condition is imposed to ensure adequate spacing between the random misorientation pairs—that is, being separated by a distance > 1% of the maximum map extent (all-points data) or being separated by a distance greater than the maximum caliper diameter of the largest grain (one-point-per-grain data). The all-points data produce distinct peaks at 2° and 65° misorientation angle (Figure 4B) due to the increased likelihood of sampling two orientations from within either of the two large olivine porphyroclasts. Consequently, the bulk A-type CPO appears becomes obscured and the all-points data produce an M value (M = 0.109) lower than that provided by the one-point-per-grain data (M = 0.131). However, it cannot be assumed that the all-points data will always produce lower CPO intensities than the one-point-per-grain data. Consider the case in which a coarse-grained, strongly textured aggregate contains a small fraction of fine, randomly oriented grains. In this case, the volumetrically dominant grain population will introduce bias towards larger CPO intensity values; thus, the all-points (area-weighted) data will yield a greater value of CPO intensity than the one-point-per-grain data.

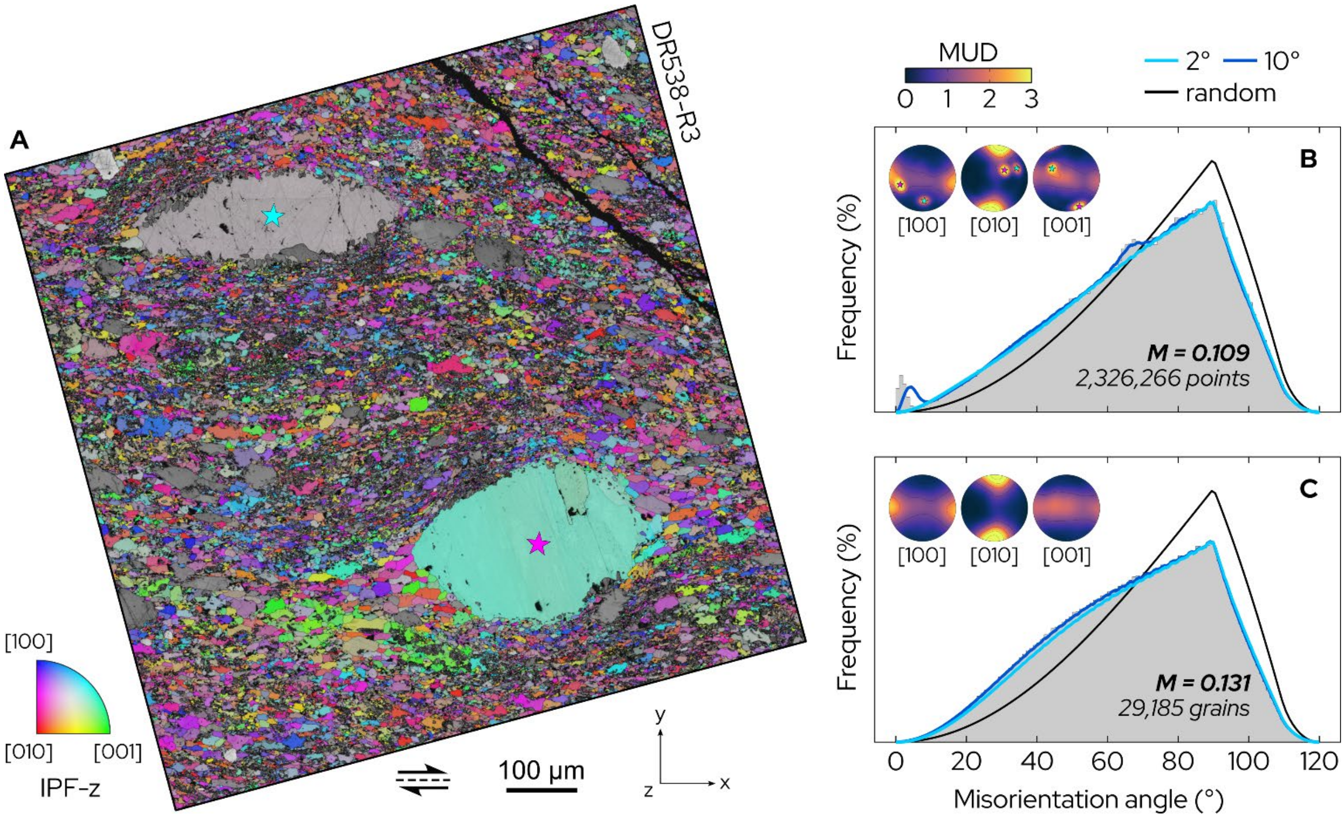

Figure 4: Comparison of all-points versus one-point-per-grain CPO data for a porphyroclastic abyssal peridotite mylonite, DR538-R3. (A) An inverse pole figure (IPF) map showing crystal orientations relative to the z-direction. (B–C) Random-pair misorientation angle histograms and contoured pole figures for the (B) all-points and (C) one-point-per-grain data. The theoretical random angle distribution is shown in black. For comparison, angle distributions derived from the ODF (Mainprice et al., 2015) are shown for ODF kernel halfwidths of 2° (light blue) and 10° (dark blue).

An MTEX-compatible function for calculating *M* via the original, discrete method of Skemer et al. (2005) is included here (Supplementary Code S1) and contains functionality for calculating *M* using either the all-points (EBSD pixel orientation) data or the one-point-per-grain (mean grain orientation) data. It is recommended that CPO intensities are calculated using the same data used to plot pole figures and that, either way, this choice is reported.

6. Sensitivity to population size

6.1 Numerical polycrystals

Finally, we can also examine how the apparent CPO intensity varies with population size. Figure 5 shows a Monte Carlo resampling analysis of the VPSC simulations described above. First, we find the model steps that correspond to 25 evenly spaced M_{MAD} values covering the full range of 0 to 1 (i.e., in increments of ~0.04). Then, for each of those steps, we recalculate M_{MAD} for 1000 random subsamples of orientations at each of 10 different population sizes, spaced evenly in logarithmic space between N = 5 and N = 20,000. Put simply, we recalculate M_{MAD} 250,000 times as a function of CPO intensity and population size. Note that we only calculate M_{MAD} as it is difficult to define a singular value of M_{ODF} and, in particular, J_{ODF}, to use as a reference measure of the "true" CPO intensity at each set of conditions.

Figures 5A–C and 5D–F show the resampling analysis results for our olivine (Figure 2) and ice (Figure 3) VPSC simulations, respectively. For CPOs of any given intensity, M_{MAD} decreases with increasing population size, converging with the true M_{MAD} value, M', at population sizes on the order of N = 100 to N = 1,000 (Figures 5A and 5D). However, there is much greater relative change in M_{MDF} for weaker CPOs—random orientation distributions ($M' \approx 0$) give M values that, on average, decrease by > 99% (i.e., from ~0.75 to ~0) as N increases, whereas strongly unimodal orientation distributions ($M' \approx 1$) give M values that decrease by only ~3% (i.e., from ~0.99 to ~0.96). To further quantify these observations, we calculate the probability, P, of obtaining the true value, M', from the normal distribution of M values produced at each set of resampling conditions, within a given degree of acceptable uncertainty, ϵ (i.e., ± 10 % for the following analyses):

$$P(M' - \epsilon \le M \le M' + \epsilon) \quad (5)$$

where P is calculated using the cumulative distribution function (CDF) of a normal distribution, φ_M—with mean, μ_M, and standard deviation, σ_M, describing the distribution of resampled M values (Figures 5A, 5D)—from z-scores corresponding to the desired bounds, $M' \pm \epsilon$:

$$P = \varphi_M(z_{\mathrm{upper}}) - \varphi_M(z_{\mathrm{lower}}) \quad (6)$$

where

$$z_{\mathrm{upper}} = \frac{M' + \epsilon - \mu_M}{\sigma_M}, \qquad z_{\mathrm{lower}} = \frac{M' - \epsilon - \mu_M}{\sigma_M} \quad (7)$$

For example, Figure 5A shows that resampling an A-type olivine CPO with $M' = 0.32$ produces a normal distribution of M values with mean, $\mu_M = 0.437$ and standard deviation, $\sigma_M = 0.0730$ when only 13 orientation measurements are selected at random each time. Thus, the probability of obtaining $M' = 0.32 \pm 0.032$ (i.e., ± 10%) is given by the z-scores, $z_{\mathrm{upper}} = -1.164$ and $z_{\mathrm{lower}} = -2.041$, corresponding to $P = 0.105$. In other words, there is a ~10.5% chance of obtaining an accurate value of M (i.e., within ±10% of M') when describing that CPO using N = 13 arbitrary orientation measurements. It is not until $N > 351$ that M' can be obtained with >95% likelihood from a single sample of orientations.

Figures 5B and 5E show the probability of obtaining $M = M'$ (within ± 10%) when sampling orientation distributions of varying CPO intensities and with varying numbers of measurements. To illustrate these data in a more intuitive manner, Figures 5C and 5F present contoured heat maps showing the number of orientation measurements required to obtain a robust measure of M at a particular probability level for various values of M'. Note that little difference is found between the VPSC simulations for olivine and ice, despite the higher symmetry class of the latter.

Generally speaking, the number of measurements required to obtain an accurate value of M decreases markedly as CPO intensity increases—consider that only a single orientation measurement would be required to describe the CPO intensity of a monodisperse (single crystal) orientation distribution with 100% likelihood of obtaining the true value, M'. Interestingly, very weak but non-random orientation distributions require the largest number of measurements to obtain a robust measure of M—to obtain a value of M with 95% probability of falling within ±10% of M', up to ~2,500 measurements are required for an A-type olivine CPO with $M' = 0.05$ (Figure 5C) while ~4,000 measurements are required for a basal-⟨a⟩ ice CPO with $M' = 0.05$ (Figure 5F). For random orientation distributions ($M \approx 0$), there is rapid convergence with M' beyond ~300 measurements (Figures 5B, 5E).

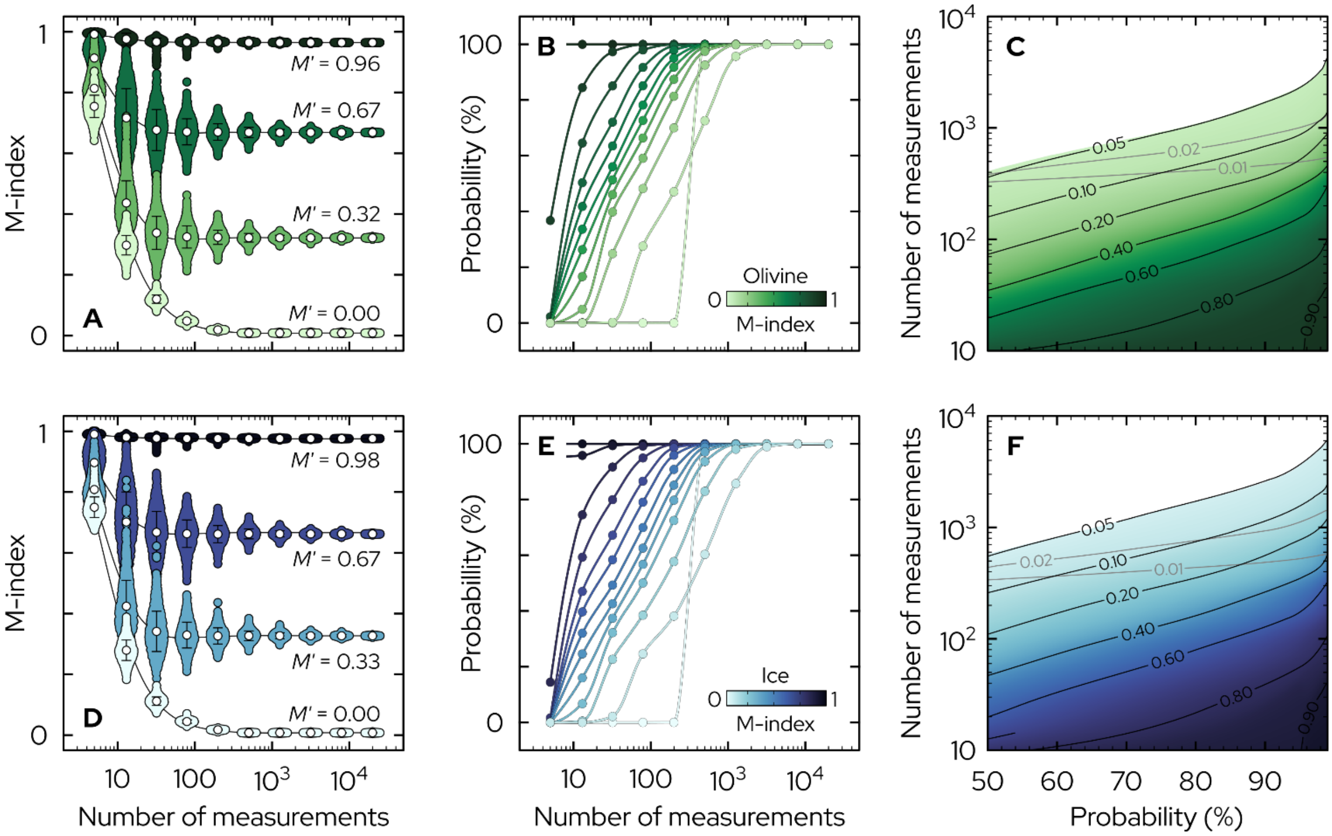

Figure 5: M-index, M_{MAD}, as a function of population size and true CPO intensity, M', for the (A–C) olivine and (D–F) ice VPSC simulations shown above. (A,D) Monte Carlo calculations of M_{MAD} for orientation distributions of varying intensity and size. For each set of conditions, M_{MAD} is calculated using 1,000 random samples of N orientations. To better show the distribution of M_{MAD}, the data points are jittered in the x-direction according to a kernel density estimate along the y-direction. The mean of each distribution is shown by a white circle, with error bars corresponding to the 1-sigma standard deviation. (B,E) The probability of obtaining an estimate of M within 10% of the true CPO intensity, M', as a function of CPO intensity and the number of orientation measurements. (C,F) Contour plots showing the number of orientation measurements required to reach a certain probability of obtaining M within ±10% of M'.

6.2 Natural and experimental samples

To test the observations reported above for the VPSC simulations, we can turn to real-world data from natural and experimental specimens. Eight specimens containing minerals of various crystal symmetry classes have been selected for analysis, as summarized in Table 1. All of the specimens had previously been mapped using EBSD, and were selected for analysis on the basis that they 1) cover a wide range of CPO intensity and symmetry, and 2) contain ≥ 5000 grains to ensure a robust measure of CPO. For consistency, a reference M-index value, *M′*, was calculated for each specimen using original histogram-based approach of Skemer et al. (2005) and the mean orientation of 5,000 grains selected at random. In order of decreasing CPO intensity, the specimens are as follows:

1) Sample PT303 is an iron-rich olivine polycrystal deformed to a shear strain of $\gamma = 3.9$ in a torsional geometry using a triaxial gas-medium Paterson apparatus at 1200°C, 300 MPa confining pressure, and a rotation rate corresponding to $2.3 \times 10^{-4}\ s^{-1}$ shear strain rate at the outer radius of the sample, where a strong A-type CPO is found (Qi et al., 2021);
2) UM1787 is a quartz-rich mylonite from the Garhwal Himalayas, India, composed primarily of quartz, biotite, muscovite, garnet, and ilmenite (Shivaji, 2020). The sample was mapped perpendicular to foliation and parallel to lineation using a ThermoFisher Helios Hydra 5 scanning electron microscope (SEM) equipped with an Oxford Instruments Symmetry S3 EBSD detector at the Marine Biological Laboratory (Woods Hole, MA, USA). Due to the relatively weak diffraction patterns produced by mica, the muscovite-dominated map was re-indexed using Oxford Instruments' MapSweeper pattern matching toolbox using the same procedures described by Hao et al. (2024), with a cross-correlation coefficient threshold of $R = 0.25$. Muscovite exhibits a strong (001)-fibre CPO, with [100] and [010] axes girdled within the foliation plane;

3) Sample PIL267 is a polycrystalline ice sample deformed in a general shear geometry in a cryogenic, triaxial gas-medium apparatus at −30°C and $1.67 \times 10^{-5}\ s^{-1}$ shear strain rate to a finite shear strain of $\gamma = 1.1$ (Fan et al., 2021b). Under these conditions, ice develops a strong (0001)-axis maximum perpendicular to the shear plane, with a subsidiary (0001)-axis maximum rotated ~45° towards the shear direction, to promote dislocation glide on the basal-⟨a⟩ slip system;

4) Sample W1794 is an intermediate-composition plagioclase polycrystal deformed in a general shear geometry using a Tullis-modified Griggs apparatus at 1000°C, 1000 MPa confining pressure, and various shear-strain-rate steps in the range 10^{-6}–$10^{-4}\ s^{-1}$ (Meyers et al., 2013). The sample was mapped using a Zeiss Sigma variable-pressure SEM equipped with an Oxford Instruments NordlysNano EBSD detector at the University of Otago (Dunedin, New Zealand);

5) DR538-R3, described above in section 5;

6) STO-2-03 is a quartz-rich mylonite from the Alpine Fault zone, New Zealand, deformed in a reverse dip-slip transpressional geometry under mid-crustal conditions (Cross et al., 2015). Quartz exhibits an asymmetric type-I cross girdle CPO due to combined basal-⟨a⟩, rhomb-⟨a⟩, and prism-⟨a⟩ slip;

7) Sample LVT128 is a specimen of Carrara marble deformed in a torsional geometry using a Large Volume Torsion (LVT) apparatus at 700°C, ~1.5 GPa confining pressure, and a rotation rate corresponding to a shear strain rate of $4.8 \times 10^{-5}\ s^{-1}$ at the outer radius of the sample (Skemer et al., 2025). A maximum shear strain of $\gamma = 3.2$ was reached at the outer radius of the sample, where calcite developed a multi-modal CPO due to combined

slip on the $c(0001)\langle\bar{1}2\bar{1}0\rangle$, $r^{+}\{10\bar{1}4\}\langle\bar{2}021\rangle$, and $r^{+}\{10\bar{1}4\}\langle20\bar{2}\bar{1}\rangle$ slip systems (Cross & Skemer, 2017);

8) Sample San466 is a fine-grained quartz polycrystal that was formed by pressurizing a quartz single-crystal into the coesite stability field and then back to the α-quartz stability field at a temperature of ~600°C using a Deformation-DIA apparatus (Goddard et al., 2025). Quartz has a macroscopically random CPO, but exhibits a crystallographic signature—where neighbouring clusters of grains have [c] axes that are misoriented by a ~84° rotation around a common $\{m\}$ axis—due to epitaxy across the coesite-quartz phase transformation (Goddard et al., 2025).

Table 1: Summary of EBSD data from natural and experimental specimens

Sample name	**Sample type**	**Phase of interest**	**Symmetry class**	**# grains**	**CPO type**	**Slip system**	***M′***
PT303	Experimental	Olivine	Orthorhombic	6210	Unimodal	A-type; (010)[100]	0.440
UM1787	Natural	Mica	Monoclinic	5590	Fibre	C-fibre; (001)[uv0]	0.268
PIL267	Experimental	Ice	Hexagonal	21924	Unimodal	Basal-a; $(0001)\langle\bar{1}2\bar{1}0\rangle$	0.217
W1794	Experimental	Plagioclase	Triclinic	6746	Unimodal	(010)[100]	0.132
DR538-R3	Natural	Olivine	Orthorhombic	29185	Bimodal	A-type with minor B-type; (010)[100], (010)[001]	0.131
STO-2-03	Natural	Quartz	Trigonal	11671	Cross-girdle	Basal-a, rhomb-a, prism-a $(0001)\langle\bar{1}2\bar{1}0\rangle$, $\{10\bar{1}1\}\langle\bar{1}2\bar{1}0\rangle$, $\{0\bar{1}11\}\langle\bar{1}2\bar{1}0\rangle$ $\{10\bar{1}0\}\langle\bar{1}2\bar{1}0\rangle$	0.043
LVT128	Experimental	Calcite	Hexagonal	7155	Multimodal	Basal-a with ±rhomb slip; $(0001)\langle\bar{1}2\bar{1}0\rangle$, $\{10\bar{1}4\}\langle\bar{2}021\rangle$, $\{10\bar{1}4\}\langle20\bar{2}\bar{1}\rangle$	0.039
San466	Experimental	Quartz	Trigonal	7752	Multimodal	N/A	0.017

All of the EBSD maps were processed using the open-source MTEX toolbox for MATLAB (Bachmann et al., 2010). To demonstrate the diverse range of CPO types present in the samples, the eigenvalue method of Vollmer (1990) was used to classify the extent to which specific crystal axes belong to point (P), girdle (G), or random (R) distributions. Figure 6A shows the P-G-R distribution of the dominant Burgers vector (i.e., crystal direction parallel to the shear direction and/or lineation) for each sample, while Figure 6B shows the P-G-R distribution of the dominant glide plane (i.e., crystal axis normal to the shear plane and/or foliation). For San466, which was conducted under nominally hydrostatic conditions, the $a\langle 11\bar{2}0\rangle$ direction and $c(0001)$ pole-to-plane were used for consistency with the other quartz-rich sample, STO-2-03.

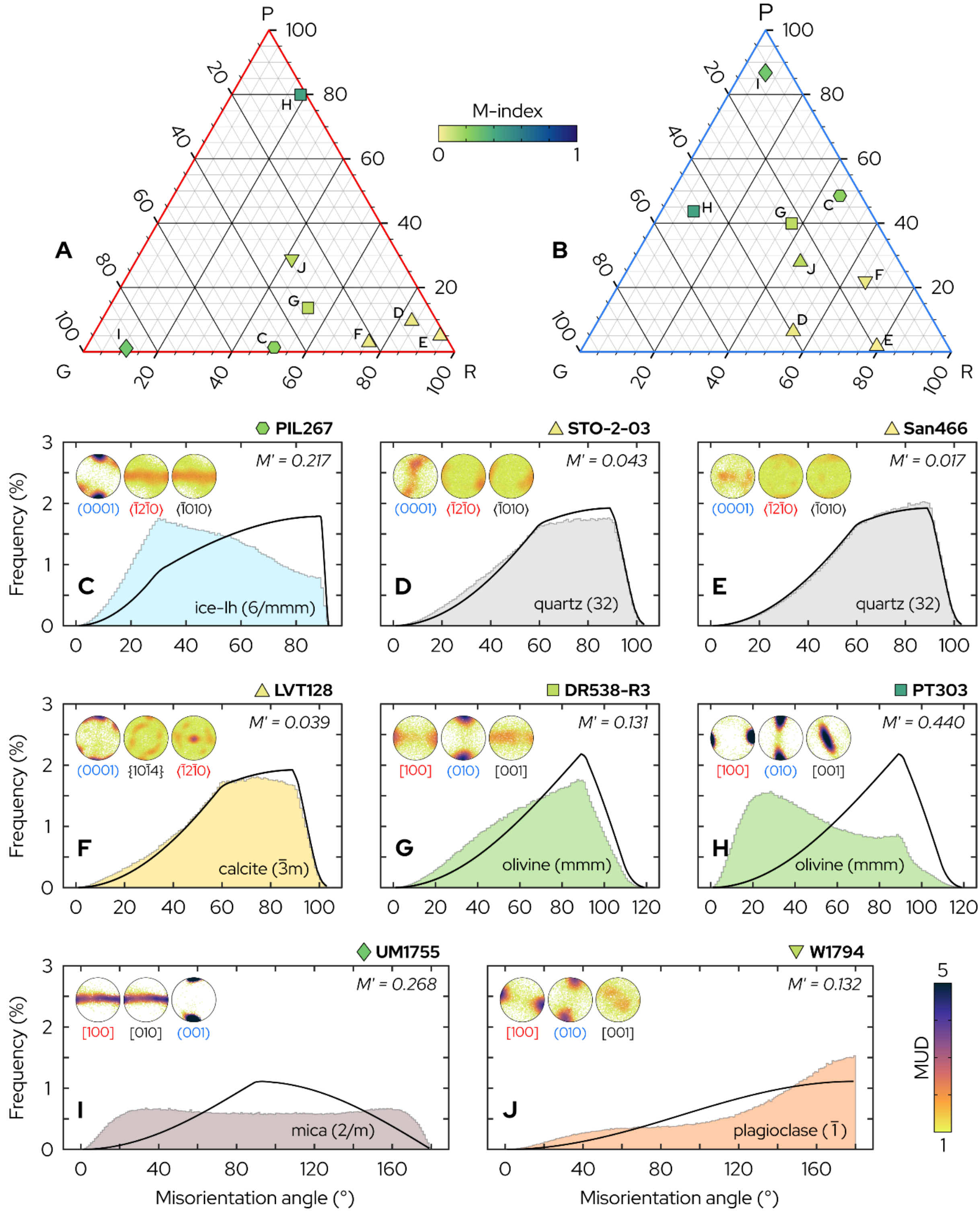

Figure 6: CPO intensity and symmetry of select natural and experimental samples. (A–B) Ternary plots, derived using the eigenvalue method of Vollmer (1990), showing the point-girdle-random CPO parameters of the (A) Burgers vectors and (B) slip planes for each sample. Each symbol is coloured according to its M-index value. (C–J) Random-pair misorientation angle histograms for each sample (shaded), compared with the corresponding theoretical misorientation angle distribution (black line) for

the corresponding crystal symmetry class. The CPO of each sample is shown using scattered pole figures (inset) where each data point is coloured by multiples of uniform distribution (MUD). The pole figures are all lower-hemisphere, equal-area projections. Sample details are provided in the main text.

The chosen samples cover almost the entire P-G-R ternary space (Figures 6A–B) and also span a wide range of CPO intensity from $M' \approx 0$ (San466) to $M' = 0.44$ (PT303) (Figures 6C–J). Thus, the samples should serve as a good test of the observations established above using VPSC modelling.

To examine the number of measurements required to obtain a representative value of CPO intensity, we can perform the same resampling analysis used above (Figure 5). Having determined that ODF-based estimates of CPO intensity are highly sensitive to their calculation parameters and that, as such, it is difficult to identify a singular reference value, the following analysis focuses solely on the original histogram-based M-index approach defined by Skemer et al. (2005).

Figure 7 shows the resampling analysis results. As expected, the probability of obtaining an M value within ±10% of the true, reference value, M', increases as more orientation measurements are provided. Furthermore, as shown for the VPSC simulations, the number of measurements required to obtain an accurate value of M increases with decreasing CPO intensity. For example, the sample with the strongest CPO, PT303 (Figure 6H), there is a 95% probability of obtaining M within ±10% of M' with only 300 orientation measurements (Figure 7A, squares), whereas

~2,000 measurements are required to reach the same probability in sample San466, which has a near-random CPO (Figure 7A, upward-facing triangles). Again, we can view these data in a more intuitive manner by plotting contoured heat maps of the number of measurements required to obtain *M*′ within a certain probability. As shown in Figure 7B, there is generally close correspondence between the heat map derived from the VPSC simulations—taken as the average of Figures 5C and 5F, given their similarity—and the real sample analyses. In general, the residual between the simulated and real data is within ±50% (Figure 7C), where positive values indicate that more measurements are required for convergence with *M*′ than suggested by the VPSC simulations, and negative values indicate that fewer measurements are required for convergence. However, there are two notable exceptions. First, the strong (001)-fibre CPO of biotite in UM1755 can be accurately described with only half the number of measurements suggested by the VPSC analyses, presumably because the girdle occupies a greater volume of orientation space, and is therefore more likely to be represented by any given orientation. Second, the very weak CPO of San466 requires far more measurements for an accurate representation of *M* than expected from the VPSC simulations—more than twice as many to obtain *M*′ with > 90% probability, in fact (Figure 7C). This discrepancy ultimately reflects the precision with which *M* can be calculated—taking 10^6 random ODFs produces a range of *M* with mean, $\mu = 0.01$, and standard deviation, $\sigma = 0.001$. Thus, any CPO characterized by $M \leq 0.01$ should be considered effectively random (i.e., $M \approx 0$).

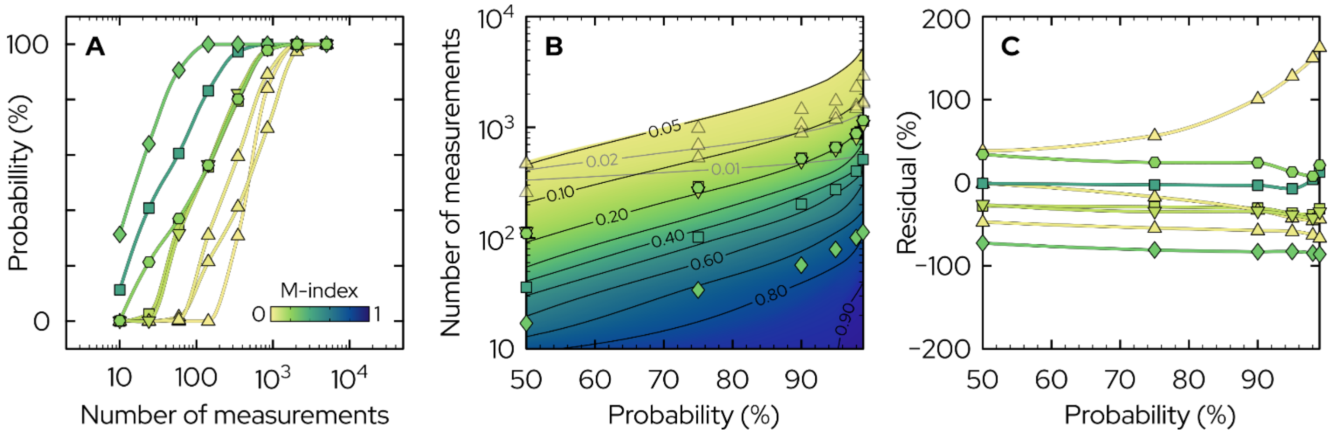

Figure 7: Resampling analysis for natural and experimental samples. (A) The probability of obtaining an estimate of *M* within 10% of the true CPO intensity, *M′*, as a function of CPO intensity and the number of orientation measurements. Symbol shapes and colours match those shown in Figure 6. (B) A contour plot showing the number of orientation measurements required to reach a certain probability of obtaining *M* within ±10% of *M′*. The heat map represents the average of Figures 5C and 5F, from the VPSC simulations. (C) The residual (i.e., misfit) between the VPSC results, represented by the heat map in (B), and the resampling analyses of the real specimens, represented by the symbols in (B). Positive values indicate that more measurements are required to obtain a measure of the "true" CPO intensity than is suggested by the VPSC simulations; negative values indicate that fewer measurements are required for a representative measure of *M* than the VPSC simulations would suggest.

For convenience, Figure 8 shows the heat map presented in Figure 7B replotted to show the number of measurements required to obtain a representative measure of M (± 10%) at varying levels of probability. Given that the VPSC simulations tend to overestimate the number of measurements required for an accurate representation of *M*—note that most samples have negative residuals in Figure 7C)—these values should be considered a conservative guide.

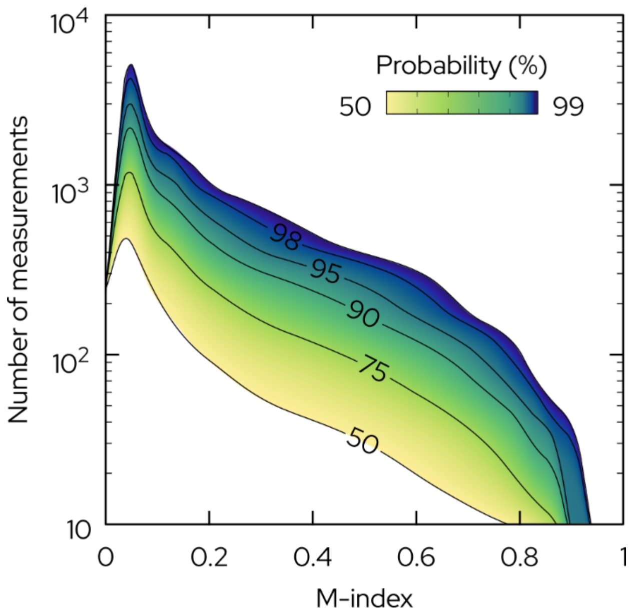

Figure 8: General guidance for the number of measurements required to accurately measure CPO intensity at various levels of probability. Heat map derived from resampling analyses of the VPSC simulations (i.e., Figures 5C and 5F). These values should be considered a conservative bound, as the real (natural and experimental) samples analysed above show convergence at smaller population sizes.

7. Closing remarks and summary

Here we have evaluated the performance of two common measures of CPO intensity, the *J*-index and the *M*-index. Both can be calculated from the orientation density function (ODF) constructed for a population of crystal orientations, such as those provided by EBSD analysis. However, the analyses above show that ODF-based scalar measures of CPO intensity can be highly unstable, can vary widely depending on the ODF construction parameters (e.g., halfwidth, bandwidth, kernel), and fail to converge to a single representative value. As such, CPO intensities reported across the literature may vary widely, even for CPOs formed under very similar conditions. Fortunately, the M-index as originally defined by Skemer et al. (2005)—that is, using the random-pair misorientation angle histogram—provides a stable, unique solution over a broad range of conditions. For convenience, a MATLAB script is provided here for calculating the M-index using the open-source MTEX toolbox and the original approach of Skemer et al. (2005).

As a general rule of thumb, it is often assumed that 200–500 measurements are required to obtain a representative estimate of microstructural "state" (e.g., grain size, CPO intensity; Humphreys, 2001; ASTM International, 2013; Cross et al., 2017b). Monte-Carlo resampling analyses show that this assumption generally holds true for CPOs of modest intensity or greater—for samples with $M \geq 0.25$, a representative estimate of M (within ±10% of the "true" value) can be obtained with 95% probability from 500 unique orientation measurements (Figure 8). However, for specimens with weak CPOs (i.e., $M < 0.1$), up to 3,000 measurements are required—significantly greater than the number of measurements recommended by Skemer et al. (2005), $N \leq 600$. However, other recent studies have recommended similarly large sample sizes for determining average grain sizes (Lopez-Sanchez & Llana-Funez, 2016; Lopez-Sanchez, 2020). Given the speed with which quantitative microstructure data (e.g., EBSD data) can now be collected (e.g., Goulden et al., 2018), such population sizes are easily attainable and should not be an impediment to robust microstructural analysis.

To close, the goal of this contribution is not to encourage the indiscriminate comparison of CPO intensity among specimens of different crystal symmetry or (de)formation history—such comparisons must always be approached with extreme caution—but to promote a clear and standardized framework for reporting CPO data. By applying consistent methods, carefully reporting analysis procedures, and adopting stable metrics such as the M-index in its original form, the community can reduce ambiguity and make results more reproducible. Such practices will not only strengthen the comparability of studies within similar geological or experimental contexts, but also help build a more robust understanding of the processes recorded by CPO formation.

Acknowledgements

This work was supported by National Science Foundation (NSF) awards OCE-2224725 and OPP-2317263 to A.J.C, and additional salary support from an Anonymous Trustee Early-Career Fellowship to A.J.C. Permission to include unpublished EBSD data was graciously provided by Tim Schroeder and Frieder Klein (specimen DR538-R3), Subhajit Ghosh and Shivaji Saha (specimen UM1787), and Cameron Meyers and Greg Hirth (specimen W1794).

Author contributions

A. J. C. designed the study, performed the analyses, and wrote the manuscript.

Data availability

The data and code used in this study will be uploaded to a public repository upon acceptance of the article for publication.

References

Andrade, E. N. da C. and Roscoe, R. (1937). Glide in metal single crystals. Proceedings of the Physical Society, 49(2), 152.

American Society for Testing and Materials. (2013). Standard Practice for Determining Average Grain Size Using Electron Backscatter Diffraction (EBSD) in Fully Recrystallized Polycrystalline Materials. ASTM International.

Azuma, N. (1994). A flow law for anisotropic ice and its application to ice sheets. *Earth and Planetary Science Letters*, *128*(3-4), 601-614.

Bachmann, F., Hielscher, R., & Schaeben, H. (2010). Texture analysis with MTEX–free and open source software toolbox. *Solid state phenomena*, *160*, 63-68.

Barreiro, J. G., Lonardelli, I., Wenk, H. R., Dresen, G., Rybacki, E., Ren, Y., & Tomé, C. N. (2007). Preferred orientation of anorthite deformed experimentally in Newtonian creep. Earth and Planetary Science Letters, 264(1-2), 188-207.

Boneh, Y., Morales, L. F., Kaminski, E., & Skemer, P. (2015). Modeling olivine CPO evolution with complex deformation histories: Implications for the interpretation of seismic anisotropy in the mantle. Geochemistry, Geophysics, Geosystems, 16(10), 3436-3455.

Bons, P. D., & Den Brok, B. (2000). Crystallographic preferred orientation development by dissolution–precipitation creep. Journal of Structural Geology, 22(11-12), 1713-1722.

Boullier, A. M., & Gueguen, Y. (1975). SP-mylonites: origin of some mylonites by superplastic flow. Contributions to Mineralogy and Petrology, 50(2), 93-104.

Bunge, H. J. (1982). *Texture analysis in materials science: mathematical methods*. Butterworths.

Bystricky, M., Kunze, K., Burlini, L., & Burg, J. P. (2000). High shear strain of olivine aggregates: Rheological and seismic consequences. *Science*, *290*(5496), 1564-1567.

Castelnau, O., Thorsteinsson, T., Kipfstuhl, J., Duval, P., & Canova, G. R. (1996). Modelling fabric development along the GRIP ice core, central Greenland. Annals of Glaciology, 23, 194-201.

Cross, A. J., Kidder, S., & Prior, D. J. (2015). Using microstructures and TitaniQ thermobarometry of quartz sheared around garnet porphyroclasts to evaluate microstructural evolution and constrain an Alpine Fault Zone geotherm. Journal of Structural Geology, 75, 17-31.

Cross, A. J., Hirth, G., & Prior, D. J. (2017a). Effects of secondary phases on crystallographic preferred orientations in mylonites. Geology, 45(10), 955-958.

Cross, A. J., Prior, D. J., Stipp, M., & Kidder, S. (2017b). The recrystallized grain size piezometer for quartz: An EBSD-based calibration. Geophysical Research Letters, 44(13), 6667-6674.

Cross, A. J., & Skemer, P. (2017). Ultramylonite generation via phase mixing in high-strain experiments. Journal of Geophysical Research: Solid Earth, 122(3), 1744-1759.

Demurtas, M., Smith, S. A., Prior, D. J., Brenker, F. E., & Di Toro, G. (2019). Grain size sensitive creep during simulated seismic slip in nanogranular fault gouges: Constraints from transmission Kikuchi diffraction (TKD). Journal of Geophysical Research: Solid Earth, 124(10), 10197-10209.

Fan, S., Cross, A. J., Prior, D. J., Goldsby, D. L., Hager, T. F., Negrini, M., & Qi, C. (2021a). Crystallographic preferred orientation (CPO) development governs strain weakening in ice: Insights from high-temperature deformation experiments. Journal of Geophysical Research: Solid Earth, 126(12), e2021JB023173.

Fan, S., Prior, D. J., Cross, A. J., Goldsby, D. L., Hager, T. F., Negrini, M., & Qi, C. (2021b). Using grain boundary irregularity to quantify dynamic recrystallization in ice. Acta materialia, 209, 116810.

Fliervoet, T. F., Drury, M. R., & Chopra, P. N. (1999). Crystallographic preferred orientations and misorientations in some olivine rocks deformed by diffusion or dislocation creep. Tectonophysics, 303(1-4), 1-27.

Goddard, R. M., Cross, A. J., Lloyd, G., Breithaupt, T., Kumamoto, K. M., Dyck, B., Chen, H., Parsons, A., Bidgood, A. (2025). A microstructural signature of the coesite-quartz transformation: New insights from high-pressure experiments and EBSD. OSF Preprints. 10.31219/osf.io/czpx5_v1

Goulden, J., Trimby, P., & Bewick, A. (2018). The benefits and applications of a CMOS-based EBSD detector. Microscopy and Microanalysis, 24(S1), 1128-1129.

Hansen, L. N., Zimmerman, M. E., & Kohlstedt, D. L. (2011). Grain boundary sliding in San Carlos olivine: Flow law parameters and crystallographic-preferred orientation. Journal of Geophysical Research: Solid Earth, 116(B8).

Hansen, L. N., Zimmerman, M. E., & Kohlstedt, D. L. (2012). Laboratory measurements of the viscous anisotropy of olivine aggregates. Nature, 492(7429), 415-418.

Hansen, L. N., Conrad, C. P., Boneh, Y., Skemer, P., Warren, J. M., & Kohlstedt, D. L. (2016). Viscous anisotropy of textured olivine aggregates: 2. Micromechanical model. Journal of Geophysical Research: Solid Earth, 121(10), 7137-7160.

Hao, M., Pommier, A., Codillo, E. A., Walter, M. J., Cross, A. J., Hrubiak, R., Wagner, L., Thomson, A. R., Yang, J., & Backhouse, N. (2024). Electrical conductivity and sound velocities of talc under high pressure and high temperature conditions and application to the subducting Cocos plate. Journal of Geophysical Research: Solid Earth, 129(11), e2024JB029824.

Humphreys, F. J. (2001). Review grain and subgrain characterisation by electron backscatter diffraction. Journal of materials science, 36(16), 3833-3854.

Karato, S. I. (1988). The role of recrystallization in the preferred orientation of olivine. Physics of the Earth and Planetary Interiors, 51(1-3), 107-122.

Karato, S. I., Jung, H., Katayama, I., & Skemer, P. (2008). Geodynamic significance of seismic anisotropy of the upper mantle: New insights from laboratory studies. *Annu. Rev. Earth Planet. Sci.*, *36*(1), 59-95.

Klein, F., Schroeder, T., John, C. M., Davis, S., Humphris, S. E., Seewald, J. S., Sichel, S., Bach, W., & Brunelli, D. (2024). Mineral carbonation of peridotite fueled by magmatic degassing and melt impregnation in an oceanic transform fault. Proceedings of the National Academy of Sciences, 121(8), e2315662121.

Lebensohn, R. A., & Tomé, C. N. (1993). A self-consistent anisotropic approach for the simulation of plastic deformation and texture development of polycrystals: application to zirconium alloys. Acta metallurgica et materialia, 41(9), 2611-2624.

Lopez-Sanchez, M. A., & Llana-Fúnez, S. (2016). An extension of the Saltykov method to quantify 3D grain size distributions in mylonites. Journal of Structural Geology, 93, 149-161.

Lopez-Sanchez, M. A. (2020). Which average, how many grains, and how to estimate robust confidence intervals in unimodal grain size populations. Journal of Structural Geology, 135, 104042.

Mainprice, D., & Nicolas, A. (1989). Development of shape and lattice preferred orientations: application to the seismic anisotropy of the lower crust. *Journal of Structural Geology*, *11*(1-2), 175-189.

Mainprice, D., Bachmann, F., Hielscher, R., & Schaeben, H. (2015). Descriptive tools for the analysis of texture projects with large datasets using MTEX: strength, symmetry and components. *Geological Society, London, Special Publications*, *409*(1), 251-271.

Meyers, C. D., Hirth, G., Cross, A. J., & Prior, D. J. (2013). The effect of dynamic recrystallization and LPO formation on deformation mechanisms in experimentally deformed plagioclase aggregates. In AGU Fall Meeting Abstracts (Vol. 2013, pp. T53A-2557).

Miranda, E. A., Hirth, G., & John, B. E. (2016). Microstructural evidence for the transition from dislocation creep to dislocation-accommodated grain boundary sliding in naturally deformed plagioclase. Journal of Structural Geology, 92, 30-45.

Miyazaki, T., Sueyoshi, K., & Hiraga, T. (2013). Olivine crystals align during diffusion creep of Earth's upper mantle. Nature, 502(7471), 321-326.

Molinari, A., Canova, G. R., & Ahzi, S. (1987). A self-consistent approach of the large deformation polycrystal viscoplasticity. Acta Metallurgica, 35(12), 2983-2994.

Pozzi, G., De Paola, N., Holdsworth, R. E., Bowen, L., Nielsen, S. B., & Dempsey, E. D. (2019). Coseismic ultramylonites: An investigation of nanoscale viscous flow and fault weakening during seismic slip. Earth and Planetary Science Letters, 516, 164-175.

Précigout, J., & Hirth, G. (2014). B-type olivine fabric induced by grain boundary sliding. Earth and Planetary Science Letters, 395, 231-240.

Qi, C., Zhao, Y. H., Zimmerman, M. E., Kim, D., & Kohlstedt, D. L. (2021). Evolution of microstructural properties in sheared iron-rich olivine. Journal of Geophysical Research: Solid Earth, 126(3), e2020JB019629.

Rathmann, N. M., Mosegaard, K., Bekkevold, I. M., Lilien, D. A., & Prior, D. J. (2024). A spectral directors method for modeling the coupled evolution of flow and CPO in polycrystalline olivine. Geochemistry, Geophysics, Geosystems, 25(12), e2024GC011831.

Rutter, E. H., Casey, M., & Burlini, L. (1994). Preferred crystallographic orientation development during the plastic and superplastic flow of calcite rocks. Journal of Structural Geology, 16(10), 1431-1446.

Schaeben, H. (1997). A simple standard orientation density function: The hyperspherical de la Vallée Poussin kernel. *Physica status solidi (b)*, *200*(2), 367-376.

Shivaji, S. (2020). Tectono-metamorphic evolution of the Himalayan metamorphic rocks: Insights from the Mandakini and Madhmaheswar Ganga river valley, Northwestern India. *Doctoral dissertation*.

Skemer, P., Katayama, I., Jiang, Z., & Karato, S. I. (2005). The misorientation index: Development of a new method for calculating the strength of lattice-preferred orientation. Tectonophysics, 411(1-4), 157-167.

Skemer, P., & Hansen, L. N. (2016). Inferring upper-mantle flow from seismic anisotropy: An experimental perspective. *Tectonophysics*, *668*, 1-14.

Skemer, P., Warren, J. M., Hansen, L. N., Hirth, G., & Kelemen, P. B. (2013). The influence of water and LPO on the initiation and evolution of mantle shear zones. *Earth and Planetary Science Letters*, *375*, 222-233.

Skemer, P., Couvy, H., Cross, A. J., Littleton, J. A., & Bollinger, C. (2025). Large volume torsion (LVT) apparatuses for rock deformation at high pressure and temperature. Review of Scientific Instruments, 96(2).

Shoji, H., & Langway Jr, C. C. (1988). Flow-law parameters of the Dye 3, Greenland, deep ice core. *Annals of Glaciology*, *10*, 146-150.

Soda, Y., Harigane, Y., Kajimoto, K., & Okudaira, T. (2019). Crystallographic preferred orientations of plagioclase via grain boundary sliding in a lower-crustal anorthositic ultramylonite. International Journal of Earth Sciences, 108(6), 2057-2069.

Smith, E. C., Baird, A. F., Kendall, J. M., Martín, C., White, R. S., Brisbourne, A. M., & Smith, A. M. (2017). Ice fabric in an Antarctic ice stream interpreted from seismic anisotropy. *Geophysical Research Letters*, *44*(8), 3710-3718.

Sundberg, M., & Cooper, R. F. (2008). Crystallographic preferred orientation produced by diffusional creep of harzburgite: Effects of chemical interactions among phases during plastic flow. Journal of Geophysical Research: Solid Earth, 113(B12).

Thomas, R., Cross, A. J., Prior, D. J., Fleming, M., & Palmer, M. (2024, December). Can superplastic creep produce a crystallographic preferred orientation (CPO) in ice?. In AGU Fall Meeting Abstracts (Vol. 2024, pp. C51A-09).

Tommasi, A., Mainprice, D., Canova, G., & Chastel, Y. (2000). Viscoplastic self-consistent and equilibrium-based modeling of olivine lattice preferred orientations: Implications for the upper mantle seismic anisotropy. Journal of Geophysical Research: Solid Earth, 105(B4), 7893-7908.

Tullis, J. A. (1979). High temperature deformation of rocks and minerals. Reviews of Geophysics, 17(6), 1137-1154.

Vollmer, F. W. (1990). An application of eigenvalue methods to structural domain analysis. *Geological Society of America Bulletin*, *102*(6), 786-791.

Wheeler, J., Prior, D., Jiang, Z., Spiess, R., & Trimby, P. (2001). The petrological significance of misorientations between grains. *Contributions to mineralogy and petrology*, *141*, 109-124.

Wheeler, J. (2009). The preservation of seismic anisotropy in the Earth's mantle during diffusion creep. Geophysical Journal International, 178(3), 1723-1732.

Woodcock, N. H. (1977). Specification of fabric shapes using an eigenvalue method. *Geological Society of America Bulletin*, *88*(9), 1231-1236.

Zhang, Y., Hobbs, B. E., & Jessell, M. W. (1994). The effect of grain-boundary sliding on fabric development in polycrystalline aggregates. Journal of Structural Geology, 16(9), 1315-1325.

Supplementary Information for

Quantifying the intensity of crystallographic preferred orientation (CPO): some practical considerations and recommended practices

A. J. Cross[1*]

[1]*Department of Geology and Geophysics, Woods Hole Oceanographic Institution, Woods Hole, MA, USA*

**Corresponding author (e-mail: across@whoi.edu)*

Contents

Figure S1: The effect of bandwidth and kernel halfwidth on the orientation density function (ODF). (Top) An inverse pole figure (IPF) map showing crystal orientations relative to the z-direction, for abyssal peridotite mylonite sample DR538-R3. (Bottom) Contoured pole figures (lower hemisphere, equal area, all points) for olivine, constructed at various bandwidths, w_b, and kernel halfwidths, w_h. (Inset, lower left) Power spectral distributions for the pole figures.

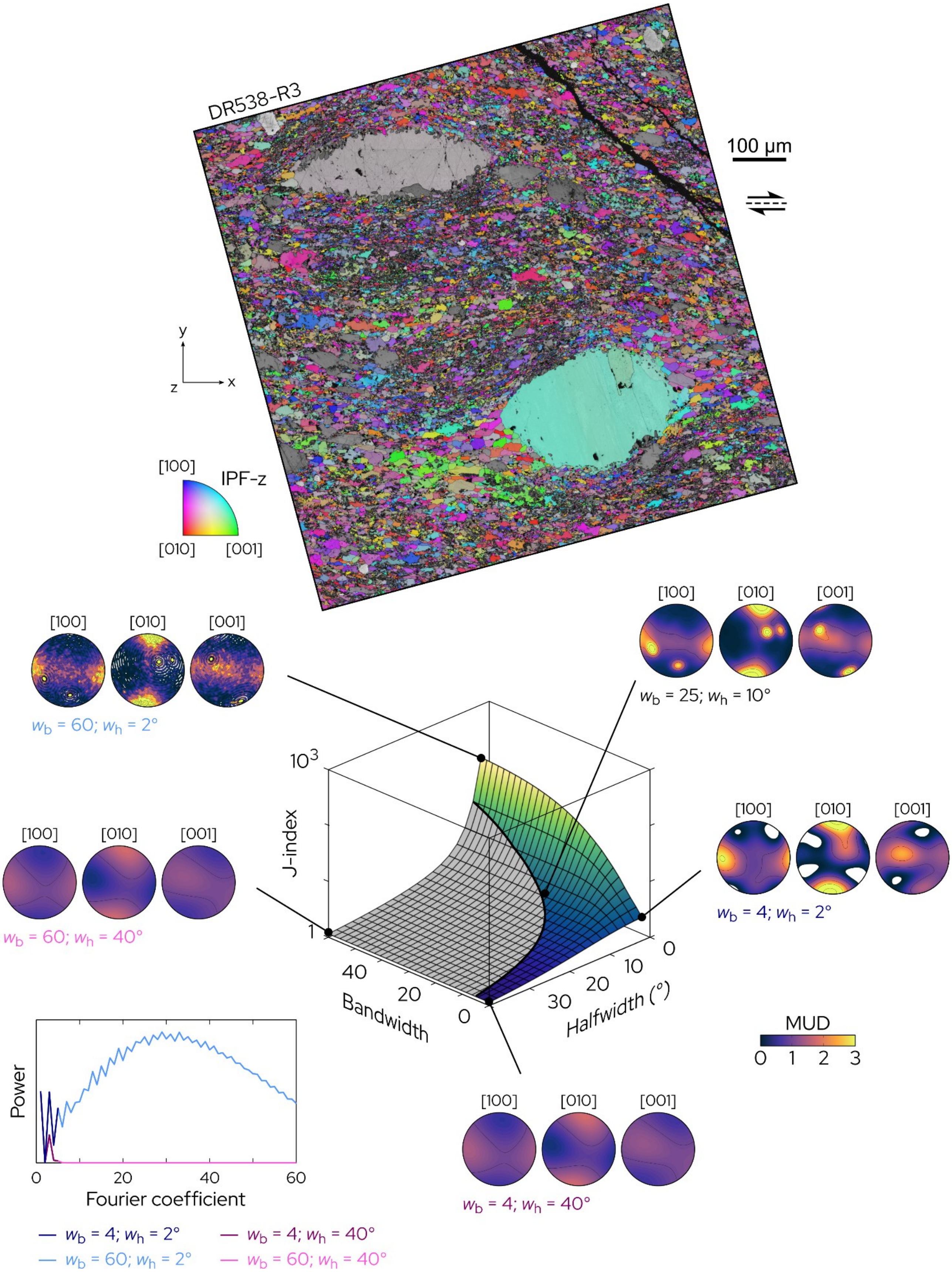

DR538-R3
100 µm
y
z
x
[100]
IPF-z
[010]
[001]
[100]
[010]
[001]
w_b = 60; w_h = 2°
[100]
[010]
[001]
w_b = 25; w_h = 10°
[100]
[010]
[001]
w_b = 60; w_h = 40°
[100]
[010]
[001]
w_b = 4; w_h = 2°
J-index
10^3
1
40
20
0
Bandwidth
0
10
20
30
Halfwidth (°)
MUD
0
1
2
3
Power
0
20
40
60
Fourier coefficient
[100]
[010]
[001]
w_b = 4; w_h = 40°
w_b = 4; w_h = 2°
w_b = 4; w_h = 40°
w_b = 60; w_h = 2°
w_b = 60; w_h = 40°

23